

## Research Article

# Surface Modification of Activated Carbon Fibers with $\text{Fe}_3\text{O}_4$ for Enhancing Their Electromagnetic Wave Absorption Property

Xuefeng Yan,<sup>1,2</sup> Tao Ji<sup>1,2</sup> and Wei Ye<sup>1,2</sup>

<sup>1</sup>National & Local Joint Engineering Research Center of Technical Fiber Composites for Safety and Health, Nantong University, Nantong 226019, China

<sup>2</sup>College of Textiles and Clothing, Nantong University, Nantong 226019, China

Correspondence should be addressed to Tao Ji; [ji.t@ntu.edu.cn](mailto:ji.t@ntu.edu.cn) and Wei Ye; [247173958@qq.com](mailto:247173958@qq.com)

Received 26 July 2020; Revised 27 September 2020; Accepted 4 November 2020; Published 2 December 2020

Academic Editor: Bhanu P. Singh

Copyright © 2020 Xuefeng Yan et al. This is an open access article distributed under the Creative Commons Attribution License, which permits unrestricted use, distribution, and reproduction in any medium, provided the original work is properly cited.

In this study, the porous activated carbon fiber (ACF) is prepared by viscose fiber, and  $\text{Fe}_3\text{O}_4$  coating is deposited on the surface of ACF through in situ hybridization to prepare carbon/magnetic electromagnetic (EM) wave absorption materials. Compared with pure  $\text{Fe}_3\text{O}_4$  and ACF, the EM wave absorption rate is improved. When the solubility of  $\text{FeCl}_3$  is 2 mol/L and the thickness of the prepared ACF- $\text{Fe}_3\text{O}_4$ (3) EM wave absorption material is 3 mm, the EM wave loss at 10 GHz reaches -44.3 dB and effective EM wave absorption bandwidths (reflection loss (RL) < -10 dB and RL < -20 dB) reached 4.8 GHz (8.8–13.6 GHz) and 1.1 GHz (9.3–10.4 GHz), respectively. The prepared ACF-based composite material has a light structure and strong absorption bandwidth. Findings can provide references for the research on other EM wave-absorbing materials.

## 1. Introduction

Given the rapid development of electronic and electrical technologies, the scope of electromagnetic (EM) energy utilization has been continuously expanded, although EM radiation pollution has followed [1–3]. The problem of EM pollution has become the fifth largest public hazard after wastewater, exhaust gas, solid waste, and noise. Relevant studies have indicated that EM pollution will replace noise pollution in the current century and become the leading physical pollution. At present, an effective method is to use EM wave absorption materials to reduce or eliminate EM wave pollution [4].

Compared to traditional ferrite, carbonyl iron magnetic EM wave absorption materials, carbon-based EM wave absorption materials have the advantages of being light weight, having adjustable frequency range, and with good compatibility with the organic/inorganic phase interface of the matrix [5–9]. Graphite powder, carbon black, carbon nanotubes, chopped carbon fiber, and activated carbon fiber (ACF) have been reported as carbon-based EM wave protection functional fillers [10–13]. We know that ACF has a large surface area, which is a factor that cannot be disregarded [14]. Given the numerous polar groups on the surface, multiple polarization

effects occur on the surface of EM wave-absorbing materials, thereby causing absorption attenuation owing to relaxation effects [15]. The main factor that determines the absorption characteristics of ACF is resistance, but its conductivity is high, easily reflects EM waves, and affects absorption efficiency [16–18]. Moreover, ACF and other carbon materials have extremely low magnetic permeability; hence, they have nearly no effect on magnetic signals, and achieving broadband absorption is difficult [16, 17]. Accordingly, many studies load magnetic particles on carbon materials, including graphite powder nickel plating, carbon nanotube nickel plating, and loading nanoferrite particles, to improve the EM wave absorption performance of materials [19–22].

The current study uses ACF with a large specific surface area as a substrate. In situ hybridization of the fiber to  $\text{Fe}_3\text{O}_4$  can significantly improve the EM wave absorption performance of the material. Effective EM wave protection composite materials have research significance.

## 2. Experimental Section

**2.1. Sample Preparation.** Preparation of ACF through industrial process and thermal decomposition promote in

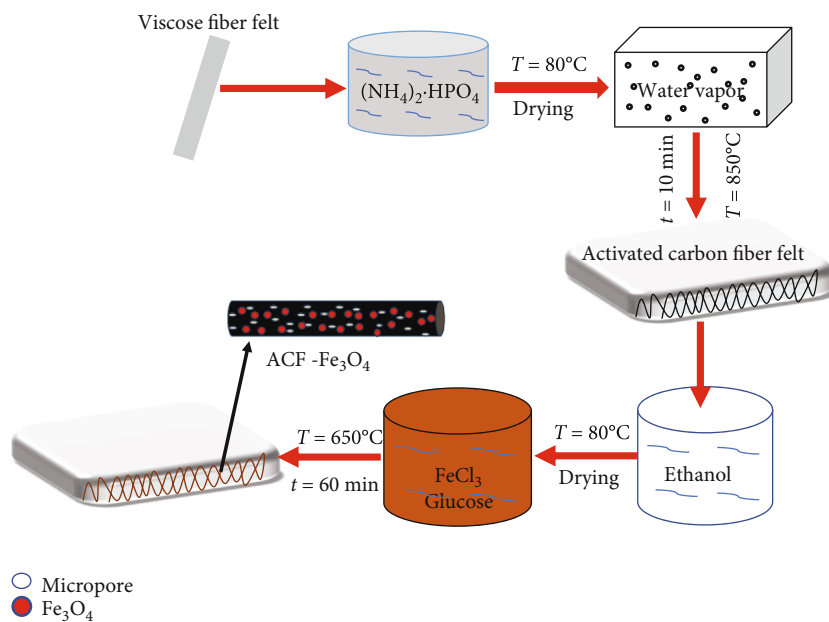


FIGURE 1: Preparation process for the ACF-Fe<sub>3</sub>O<sub>4</sub> composites.

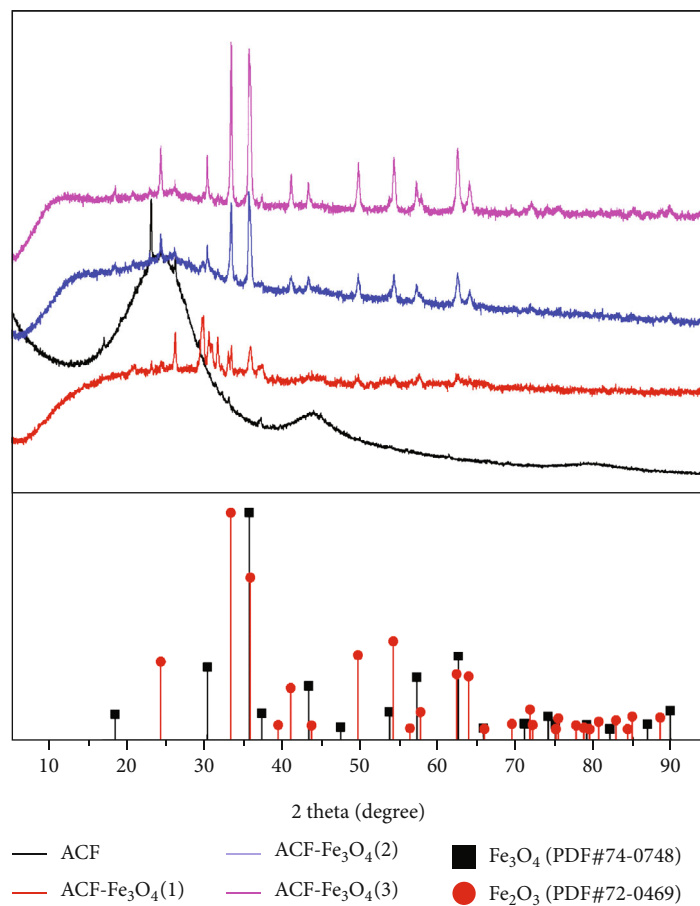


FIGURE 2: XRD profiles of ACF, ACF-Fe<sub>3</sub>O<sub>4</sub>(1), ACF-Fe<sub>3</sub>O<sub>4</sub>(2), and ACF-Fe<sub>3</sub>O<sub>4</sub>(3).

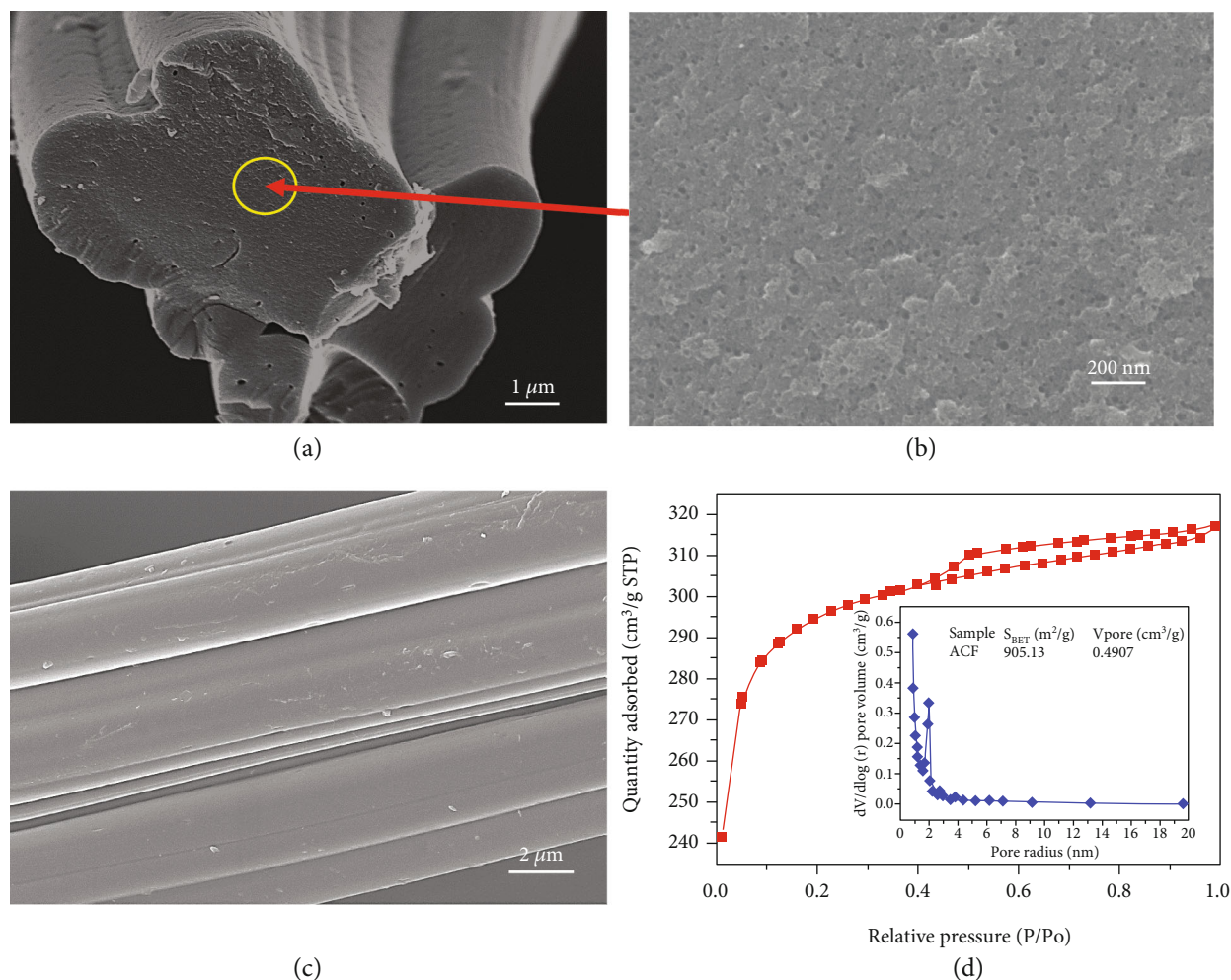


FIGURE 3: SEM images of (a, b) fiber cross-section of ACF and (c) ACF; nitrogen adsorption isotherm and pore size distribution of (d) ACF.

situ growth of  $\text{Fe}_3\text{O}_4$  on the surface of ACF, and the process route is shown in Figure 1. In detail, the viscose fiber is impregnated with ammonium hydrogen phosphate, dried, and treated at  $850^\circ\text{C}$  for 10 minutes; the process is passed through steam to prepare ACF. 0.25 mol glucose was dissolved into 1000 mL distilled water followed by the addition of 2 mol  $\text{FeCl}_3$  to form a homogeneous solution. ACF felt was added to the solution, in which the rolling surplus rate was 900%. After drying, ACF that contained  $\text{FeCl}_3$  was heat-treated at  $650^\circ\text{C}$  for 60 min in  $\text{N}_2$  gas, covered the ACF surface with a layer of  $\text{Fe}_3\text{O}_4$ , and prepared ACF- $\text{Fe}_3\text{O}_4$ (3). The amount of  $\text{Fe}_3\text{O}_4$  in the composites was regulated by the addition of different amounts of  $\text{FeCl}_3$  and glucose, specifically 0, 0.5, and 1 mol for  $\text{FeCl}_3$  and 0, 0.0625, and 0.125 mol for glucose. By using the preceding experimental method, the final products were denoted as ACF, ACF- $\text{Fe}_3\text{O}_4$ (1), and ACF- $\text{Fe}_3\text{O}_4$ (2), respectively.

**2.2. Characterization.** Phase structural analysis of the prepared ACF- $\text{Fe}_3\text{O}_4$  was performed using X-ray diffraction

(XRD; Rigaku D/max-2500PC) with  $\text{CuK}\alpha$  radiation. A scanning electron microscope (SEM; ZEISS Gemini SEM 300) equipped with an energy dispersive spectrometer (EDS) was used for morphological observations and elemental analyses. Textural characterization was carried out by nitrogen adsorption at 77 K using an ASAP 2020 automatic physisorption analyzer (Micromeritics Instrument Corp., USA). The chemical states were characterized by X-ray photoelectron spectroscopy (XPS; Thermo Fisher Scientific ESCALAB-250) with  $\text{Cu K}\alpha$  radiation. The magnetic properties were achieved using a vibrating sample magnetometer (VSM; Quantum Design MPMS) at 300 K. The formation mechanism was analyzed using thermogravimetry/differential scanning calorimetry (TG/DSC; Netzsch 214 Polyma) at a heating rate of  $10^\circ\text{C}/\text{min}$  from  $30^\circ\text{C}$  to  $1000^\circ\text{C}$  in the presence of air. The EM parameters (i.e., relative complex permittivity and relative complex permeability) were evaluated using a vector network analyzer (VNA; CeyearAV3672C) in the frequency range of 2.0–18.0 GHz. Prior to the test, the sample was thoroughly mixed with paraffin at a mass ratio of 3:7 and pressed

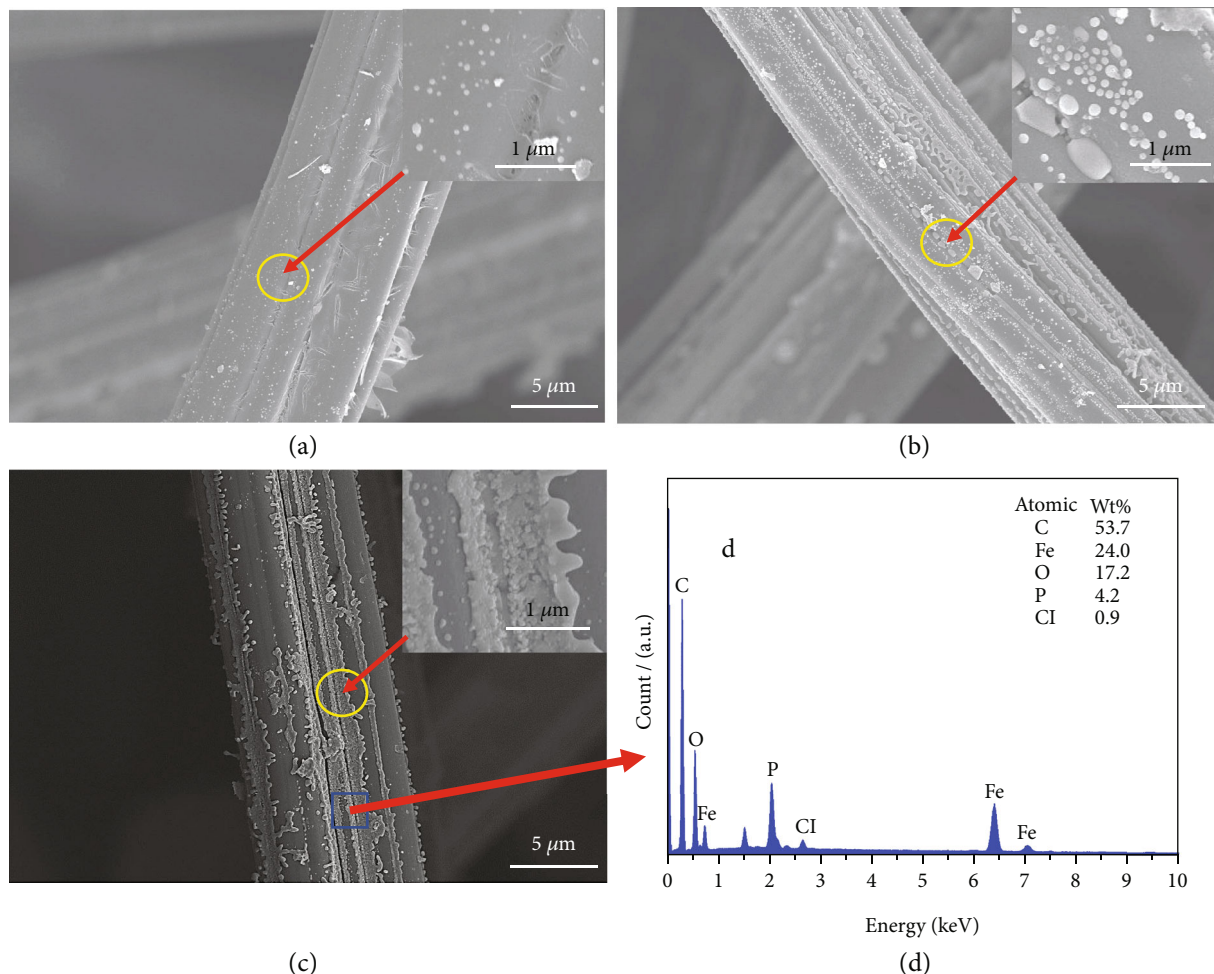
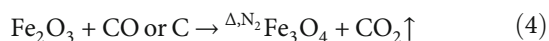
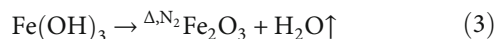
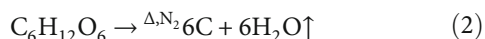
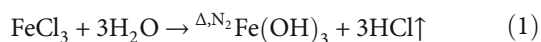


FIGURE 4: SEM images of (a) ACF-Fe<sub>3</sub>O<sub>4</sub>(1), (b) ACF-Fe<sub>3</sub>O<sub>4</sub>(2), and (c) ACF-Fe<sub>3</sub>O<sub>4</sub>(3); EDS of (d) ACF-Fe<sub>3</sub>O<sub>4</sub>(3).

thereafter into a coaxial ring with outer and inner diameters of 7 mm and 3.04 mm, respectively.

### 3. Results and Discussion

**3.1. Crystal Structure.** XRD profiles of ACF, ACF-Fe<sub>3</sub>O<sub>4</sub>(1), ACF-Fe<sub>3</sub>O<sub>4</sub>(2), and ACF-Fe<sub>3</sub>O<sub>4</sub>(3) are shown in Figure 2. ACF felt, FeCl<sub>3</sub>, and glucose were treated with high temperature at 650°C under the protection of nitrogen, FeCl<sub>3</sub> and glucose undergo thermal decomposition, and the reduction reaction produced Fe<sub>3</sub>O<sub>4</sub> (PDF # 74-0748) magnetic particles. The chemical reaction is shown in Eqs. (1)–(4) [23, 24]. Nonmagnetic Fe<sub>2</sub>O<sub>3</sub> (PDF # 72-0469) is also present. The diffraction peaks of ACF at 26.5° and 43.3° are typical diffraction peaks of carbonaceous fibers [21].



**3.2. Morphological and EDS Analyses.** Figures 3(a) and 3(b) show a SEM of the fiber cross-section of ACF. We found that there are many tiny pores inside the fiber, and the presence of a large number of pores means that the fiber has more interfaces. Figure 3(c) shows that the ACF surface has evident grooves, which is a typical viscose-based ACF after drawing treatment [25]. At the same time, it can be seen from the ACF N<sub>2</sub> adsorption isotherm and pore size distribution diagram (Figure 3(d)) that ACF has a large specific surface area and micropores smaller than 2.5 nm. This is because after the activation process of viscose fibers, a large number of micropores are generated, which increases the specific surface area of the fibers.

After Fe<sub>3</sub>O<sub>4</sub> is loaded, the particles tend to accumulate in the grooves on the fiber surface. Figures 4(a)–4(c) show the fiber surface morphology after being impregnated with different concentrations of the FeCl<sub>3</sub> solution and heat-treated. Fe<sub>3</sub>O<sub>4</sub> particles are distributed along the fiber axis. As the proportion of metal salts increases, the distributed particles increase and there is an aggregation phenomenon. XRD analysis shows that the particulate matter contains Fe<sub>3</sub>O<sub>4</sub>; it has EM wave absorption properties. When combined with a carbon-based material, the increase in Fe<sub>3</sub>O<sub>4</sub> can effectively increase the EM wave absorption performance

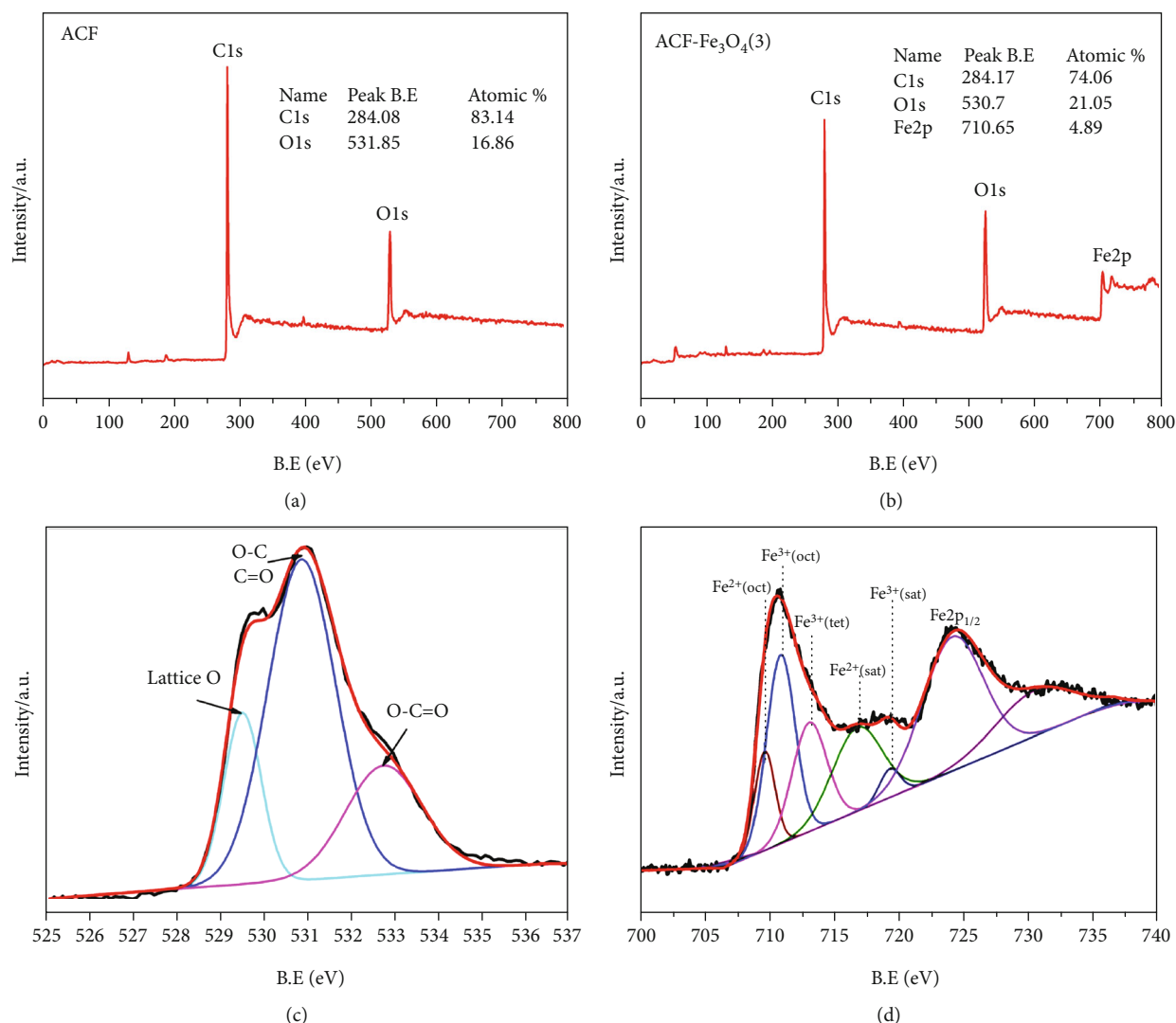


FIGURE 5: XPS spectra: wide scan of (a) ACF and (b) ACF-Fe<sub>3</sub>O<sub>4</sub>(3); (c) O1s and (d) Fe2p spectra for ACF-Fe<sub>3</sub>O<sub>4</sub>(3) composite.

of the material [26, 27]. Figure 4(d) shows the elemental analysis of the ACF-Fe<sub>3</sub>O<sub>4</sub>(3) energy dispersive spectrometer (EDS). After the in situ hybridization of Fe<sub>3</sub>O<sub>4</sub> on the ACF surface to form an ACF-Fe<sub>3</sub>O<sub>4</sub> composite, there is the presence of Fe and O elements on the fiber surface. The ACF preparation process includes the dip of ammonium dihydrogen phosphate; thus, element P is also detected. These elements constitute the Fe<sub>3</sub>O<sub>4</sub> formed in the XRD analysis, thereby further confirming the possibility of its formation. In addition, Fe<sub>3</sub>O<sub>4</sub> that absorbs EM waves forms a multi-interface structure on the fiber surface with rich interface polarization; this can promote the EM wave absorption of the material.

**3.3. XPS Analyses.** XPS will obtain more information on the composition of the ACF and ACF-Fe<sub>3</sub>O<sub>4</sub> material. Figures 5(a) and 5(b) show the X-ray photoelectron spectra of ACF and ACF-Fe<sub>3</sub>O<sub>4</sub>(3) composite. ACF consisted of the elements C and O. The ACF-Fe<sub>3</sub>O<sub>4</sub>(3) consisted of C, O, and Fe. Figure 5(c) shows the O1s XPS spectrum for

ACF-Fe<sub>3</sub>O<sub>4</sub>(3). The spectrum can fit to three peaks with binding energies of 529.50, 530.86, and 532.75 eV. The lattice oxygen at 530.86 eV is comparable to macroscaled crystallite binding energy values for magnetite [28]. The spin-orbit peaks of Fe2p<sub>1/2</sub> and Fe2p<sub>3/2</sub> are shown in Figure 5(d); Fe2p peaks at 710.89 eV and 724.46 eV are characteristic peaks of X-ray photoelectron spectroscopy [29, 30]. We found that Fe<sub>3</sub>O<sub>4</sub> is composed of three forms of iron, namely, Fe<sup>2+</sup> octahedron, Fe<sup>3+</sup> octahedron, and Fe<sup>3+</sup> tetrahedron. The Fe2p<sub>3/2</sub> derived from the binding energy of 710.89 eV was reasonably divided into peaks to obtain three main peaks and two satellite peaks. The Fe<sup>2+</sup>/Fe<sup>3+</sup> ratio is 0.63, which is slightly larger than the theoretical value of Fe<sub>3</sub>O<sub>4</sub> of 0.5, and it is due to the existence of Fe<sub>2</sub>O<sub>3</sub> [31, 32].

**3.4. TG and magnetic hysteresis analyses.** The temperature stability of microwave-absorbing materials is an important material property related to practical engineering applications. Figure 6 shows the TG analysis of the ACF and ACF-Fe<sub>3</sub>O<sub>4</sub> composites in the air at a heating rate of

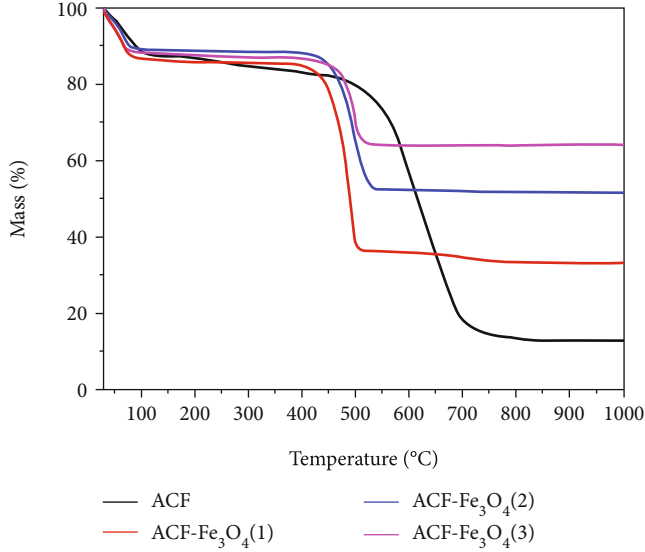


FIGURE 6: TG curves of the ACF and ACF-Fe<sub>3</sub>O<sub>4</sub> composites in the air.

10°C/min. The mass loss process is following three stages. The slight mass loss below 110°C is due to the evaporation of the sample water. Thereafter, a weight loss gradually occurred from 110°C to 410°C, which can be attributed to the removal of the unstable oxygen-containing functional groups from the sample and H<sub>2</sub>O vapor caused by the destruction of the oxidized functional groups. Lastly, ACF showed a significant weight loss between 410°C and 720°C, thereby indicating that ACF was oxidized and decomposed in the air. The apparent weight loss of the ACF-Fe<sub>3</sub>O<sub>4</sub> composite material is from 410°C to 540°C. The reason is that the presence of metal ions promotes the accelerated oxidation of ACF, while Fe<sub>3</sub>O<sub>4</sub> is oxidized to Fe<sub>2</sub>O<sub>3</sub> [33, 34].

In general, ACF-based materials have striking magnetic properties because of their fibrous structure and high specific surface area. Evidently, these characteristics can affect the magnetic properties of the material. The magnetic properties of the ACF-Fe<sub>3</sub>O<sub>4</sub> composite materials were studied at room temperature by measuring their magnetization curves. These magnetic properties include  $M_s$ ,  $M_r$ , and  $H_c$  (see Figure 7). Table 1 also shows the magnetic parameters corresponding to Figure 7. ACF has no magnetic properties, and pure Fe<sub>3</sub>O<sub>4</sub> is a typical superparamagnetic material that has high saturation  $M_s$  and  $M_r$  and low  $H_c$  [35]. As the (Fe<sub>3</sub>O<sub>4</sub>)-ACF ratio increases, the saturation and residual magnetizations of the composite material increase, while the coercive force decreases. ACF-Fe<sub>3</sub>O<sub>4</sub>(3) has high  $M_s$  (14.435 emu/g) and  $M_r$  (2.023 emu/g), while  $H_c$  (178.857 Oe) is low, at room temperature, and ACF-Fe<sub>3</sub>O<sub>4</sub> (3) is superparamagnetic. It shows that the introduction of magnetic Fe<sub>3</sub>O<sub>4</sub> causes the difference in the magnetic properties of the composite materials [26, 36].

**3.5. EM Parameters.** Figures 8(a)–8(d) show the measured dielectric properties of five samples of 30 wt% ACF, Fe<sub>3</sub>O<sub>4</sub>, and ACF-Fe<sub>3</sub>O<sub>4</sub> composites in the 2–18 GHz range. Note that samples with a high (ACF)-(Fe<sub>3</sub>O<sub>4</sub>) ratio show high

values of  $\epsilon'$  and  $\epsilon''$  in the frequency range of 2–18 GHz (see Figures 8(a) and 8(b)). For ACF-Fe<sub>3</sub>O<sub>4</sub> (2), ACF-Fe<sub>3</sub>O<sub>4</sub> (3), and pure Fe<sub>3</sub>O<sub>4</sub>, the  $\epsilon'$  value decreases insignificantly with increasing frequency in the 2–18 GHz range. Although the  $\epsilon''$  value is in the 8–14 GHz range (Figure 8(b)), the peak shows the resonance behavior, which is expected when the sample has high conductivity. Free electron theory indicates that  $\epsilon' = 1/2\epsilon_0\pi\rho f$ , where  $\epsilon'$  is the dielectric constant of vacuum,  $\rho$  is the resistivity, and  $f$  is the frequency of the microwave. The conductivity of ACF is extremely high and will form a large conductive network. Thus, the resistivity of the composite material  $\rho$  decreases, and as the ACF content increases,  $\epsilon'$  becomes considerably high. Figures 8(a) and 8(b) show that in the frequency range of 2–18 GHz, changes in the  $\epsilon'$  and  $\epsilon''$  curves of ACF and ACF-Fe<sub>3</sub>O<sub>4</sub>(1) are similar and fluctuate in the 8–12 GHz range. Figures 8(c) and 8(d) show the  $\mu'$  and  $\mu''$  values of the relative complex permeability of the ACF, Fe<sub>3</sub>O<sub>4</sub>, and ACF-Fe<sub>3</sub>O<sub>4</sub> composites. With the introduction of the Fe<sub>3</sub>O<sub>4</sub> particles, signs of magnetic increase can be observed from the enhanced permeability. For ACF and ACF-Fe<sub>3</sub>O<sub>4</sub>(1), the change trend is not substantially different because the condition is that the concentration of Fe<sub>3</sub>O<sub>4</sub> particles is relatively low. Figures 8(c) and 8(d) show that the  $\mu'$  and  $\mu''$  curves of the composite material do not fluctuate substantially, and their values are approximately 1 and 0, respectively, which are similar to those reported in the literature [37, 38]. In terms of the key factor of absorption, magnetic resonance peaks are evident near 9 GHz and 15 GHz, which are the surface effects of the magnetic particles and spin wave excitation [39]. Dielectric loss tangent ( $\tan \delta_E = \epsilon''/\epsilon'$ ) and magnetic loss tangent ( $\tan \delta_M = \mu''/\mu'$ ) can characterize the dielectric and magnetic losses of the materials. Materials absorb EM waves through two main mechanisms. We calculated  $\tan \delta_E$  and  $\tan \delta_M$  for each sample to determine which one dominates the material. We found that the material  $\tan \delta_E$  is between 0 and 0.8, while  $\tan \delta_M$  is between 0 and 0.3. Obviously, the role of dielectric loss and magnetic loss in ACF/Fe<sub>3</sub>O<sub>4</sub> composites is limited. High dielectric constant materials affect impedance matching and have strong reflection and weak absorption [40, 41]. The material itself and its structure can enhance the EM wave absorption performance of the material [42].

The Debye dipolar relaxation indicates can be expressed by the following equation [43]:

$$\epsilon_r = \epsilon_\infty + \frac{\epsilon_s - \epsilon_\infty}{1 + j2\pi f\tau} = \epsilon'(f) + i\epsilon''(f), \quad (5)$$

where  $f$  is the frequency,  $\tau$  is the relaxation time, and  $\epsilon_s$  and  $\epsilon_\infty$  are the stationary and optical dielectric constants, respectively. The following equation can be deduced from Eqn. (5):

$$\epsilon'(f) = \epsilon_\infty + \frac{\epsilon_s + \epsilon_\infty}{1 + (2\pi f)^2\tau^2}, \quad (6)$$

$$\epsilon''(f) = \frac{2\pi f\tau(\epsilon_s - \epsilon_\infty)}{1 + (2\pi f)^2\tau^2}. \quad (7)$$

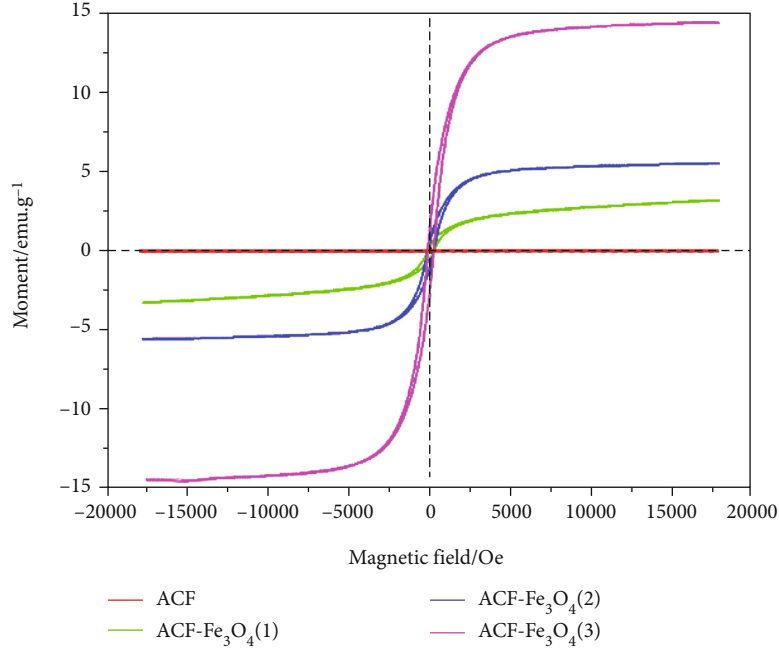


FIGURE 7: Magnetic hysteresis loops of ACF, ACF-Fe<sub>3</sub>O<sub>4</sub>(1), ACF-Fe<sub>3</sub>O<sub>4</sub>(2), and ACF-Fe<sub>3</sub>O<sub>4</sub>(3) composites.

TABLE 1: Magnetic properties of ACF, ACF-Fe<sub>3</sub>O<sub>4</sub>(1), ACF-Fe<sub>3</sub>O<sub>4</sub>(2), and ACF-Fe<sub>3</sub>O<sub>4</sub>(3) composites at room temperature.

Samples	H <sub>c</sub> (Oe)	M <sub>s</sub> (emu/g)	M <sub>r</sub> (emu/g)
ACF	207.724	0.021	0.002
ACF-Fe <sub>3</sub> O <sub>4</sub> (1)	187.913	3.212	0.392
ACF-Fe <sub>3</sub> O <sub>4</sub> (2)	177.258	5.546	0.798
ACF-Fe <sub>3</sub> O <sub>4</sub> (3)	175.857	14.435	2.023

Equations (6) and (7) indicate that the relationship between  $\epsilon'$  and  $\epsilon''$  can be deduced as follows:

$$\left(\epsilon' - \epsilon_{\infty}\right)^2 + \left(\epsilon''\right)^2 = \left(\epsilon_s - \epsilon_{\infty}\right)^2. \quad (8)$$

Figure 9 shows a plot of the  $\epsilon''$  values vs.  $\epsilon'$  values based on Eq. (8). Evidently, the ACF-Fe<sub>3</sub>O<sub>4</sub> composite material obtained seven clear parts of overlapping semicircles. This result indicates a double dielectric relaxation process in the ACF-Fe<sub>3</sub>O<sub>4</sub> composite owing to the overlapping semicircles. Accordingly, the presence of the large specific surface area ACF improves the intensity of the Debye dipole relaxation process, and the interface between ACF and Fe<sub>3</sub>O<sub>4</sub> particles is the cause of double dielectric loss. To describe the dielectric relaxation process in detail, the typical Cole-Cole curve of ACF is also shown in Figure 9. The relaxation process (multiple semicircles) of ACF is evidently caused by defects and groups. We know that ACF is prepared by viscose fiber impregnated with ammonium dihydrogen phosphate and activated by high-temperature water vapor. Numerous micropores and oxygen-containing groups will cause many defects on the ACF surface. Thereafter, defects can act as polarization centers will produce polarization relaxation

under changing EM fields and attenuate EM waves; this will have a profound impact on the loss of electromagnetic waves. Free electron theory ( $\epsilon'' = 1/2 \epsilon_0 \rho \pi f$ ) shows that the  $\epsilon''$  is proportional to the specific conductance. Pure ACF has a high conductivity, thereby resulting in a high  $\epsilon''$  value. Thus, ACF has strong dielectric loss. Therefore, the ACF arc is larger than other samples. However, the high ACF conductivity may also cause a significant skin effect because the surface is exposed to EM waves. The high  $\epsilon''$  of ACF or low  $\epsilon''$  of the Fe<sub>3</sub>O<sub>4</sub> particles may reduce the impedance matching of the material. Accordingly, pure ACF and Fe<sub>3</sub>O<sub>4</sub> particles show extremely poor microwave absorption performance, as shown in Figure 10. In our case, a new composite material was obtained using the appropriate amount of ACF and Fe<sub>3</sub>O<sub>4</sub> particles. Hence, the material can considerably respond to the impedance matching requirements while maintaining the existing dielectric relaxation characteristics.

**3.6. EM Wave-Absorbing Properties.** Figure 10 shows the RL curves of the ACF, Fe<sub>3</sub>O<sub>4</sub>, and ACF-Fe<sub>3</sub>O<sub>4</sub> composites with different thicknesses, as well as the corresponding 3D surface plots. As shown in Figures 10(a) and 10(j), the Fe<sub>3</sub>O<sub>4</sub> RL is relatively poor at frequencies between 2 GHz and 18 GHz and is above -5.0 dB in the RL range. Moreover, RL of ACF is only 0.8 GHz with a bandwidth below -10.0 dB. Dielectric loss is the main microwave absorption mechanism of ACF owing to weak magnetic properties. Previous studies have concluded that the local state close to the Fermi level can be achieved by introducing the lattice defects in the carbonaceous material and when radiation is incidental on the surface of the absorber, thereby causing a large radiation absorption. Consequently, the existence of high specific surface area and defects is an important reason for the

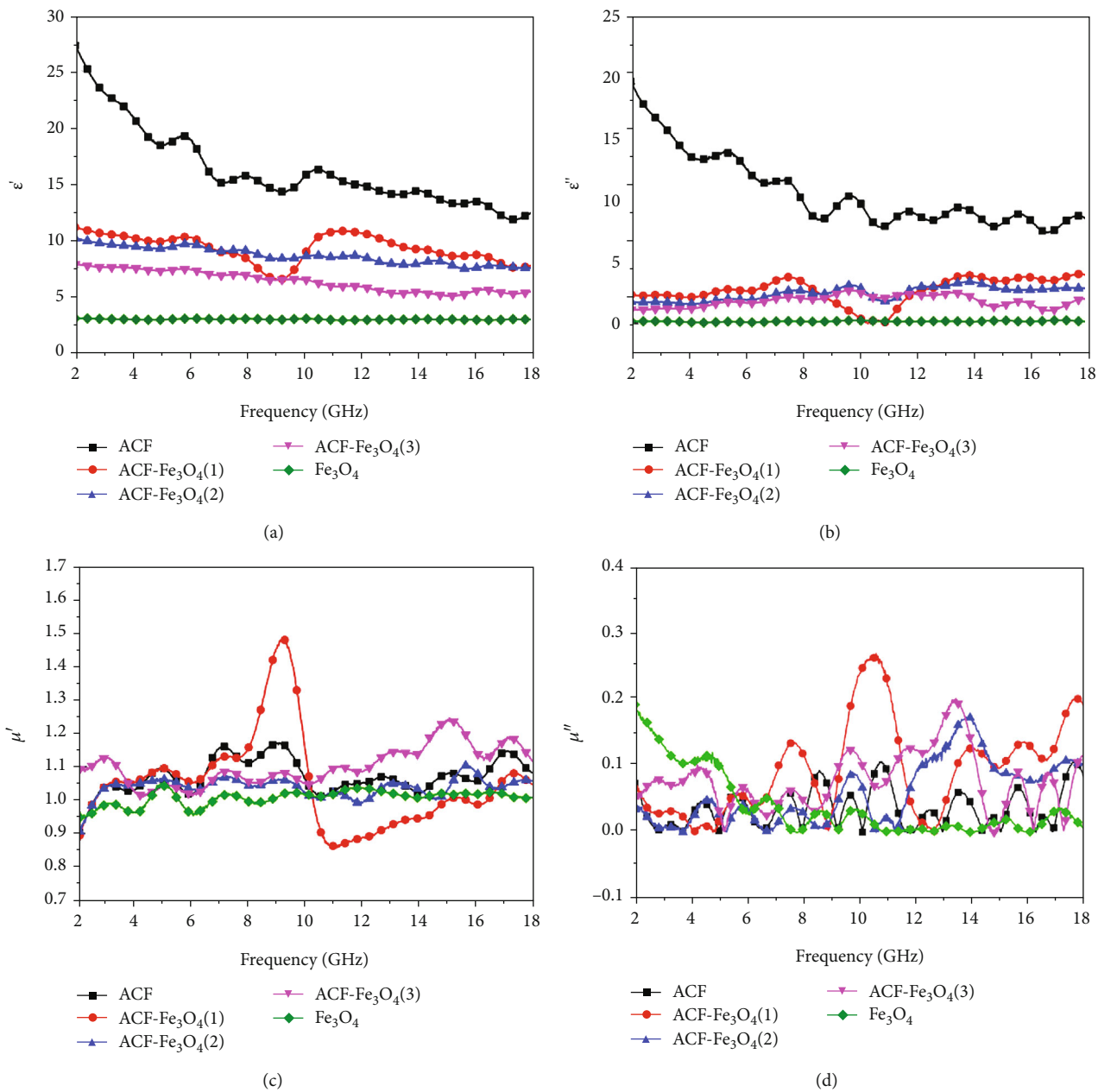


FIGURE 8: Continued.

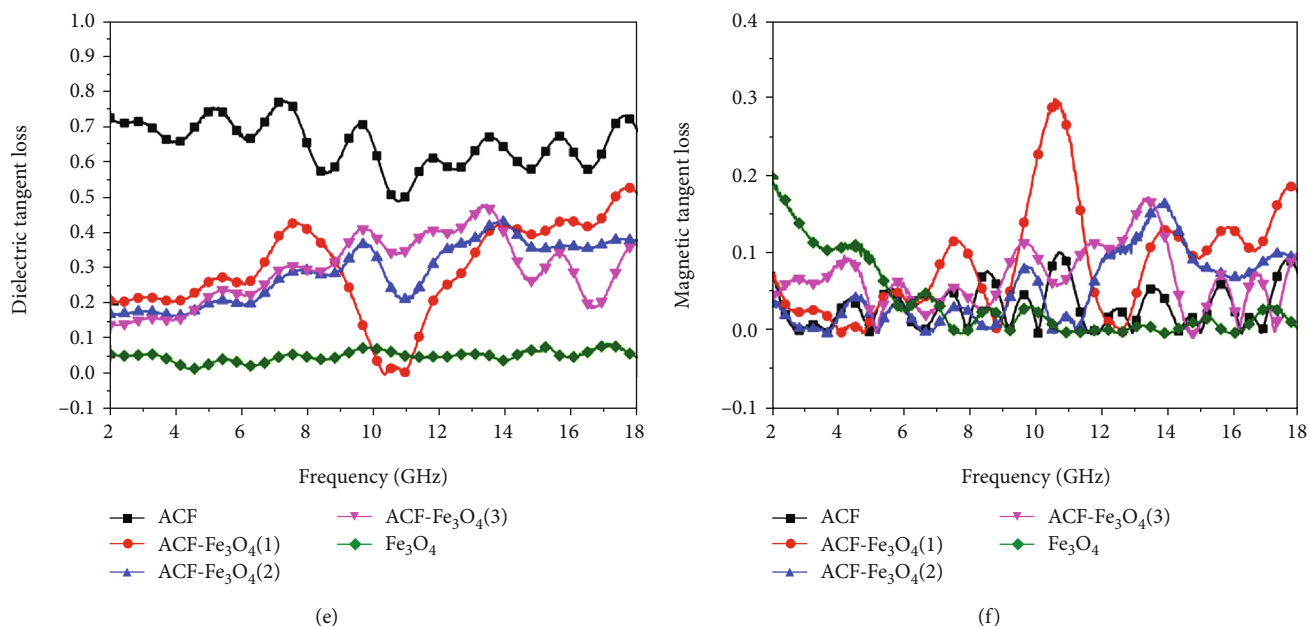


FIGURE 8: Frequency dependence on (a) real and (b) imaginary parts of the complex permittivity of samples, (c) real and (d) imaginary parts of the complex permeability, and the (e) corresponding dielectric and (f) magnetic loss tangents of ACF, ACF-Fe<sub>3</sub>O<sub>4</sub>(1), ACF-Fe<sub>3</sub>O<sub>4</sub>(2), ACF-Fe<sub>3</sub>O<sub>4</sub>(3), and Fe<sub>3</sub>O<sub>4</sub>.

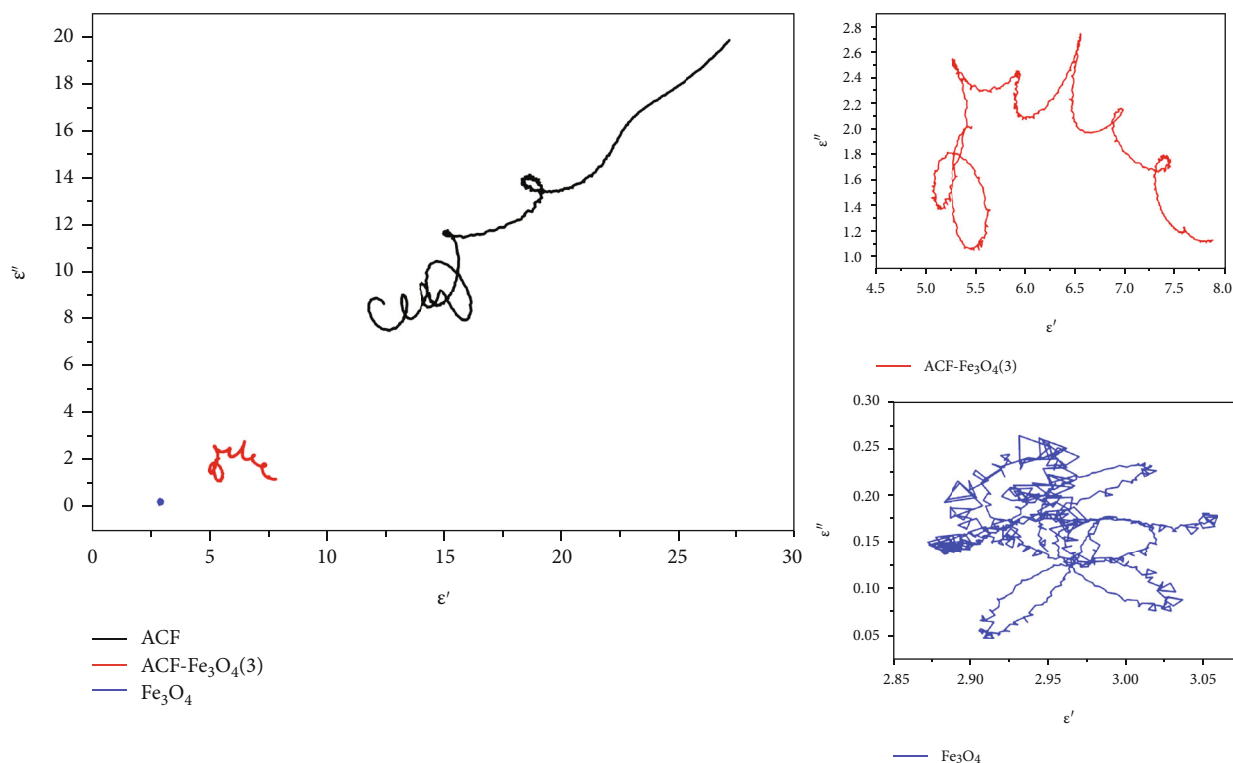


FIGURE 9: Typical Cole-Cole curves of ACF, CF-Fe<sub>3</sub>O<sub>4</sub>(3), and pure Fe<sub>3</sub>O<sub>4</sub>.

improvement of the electromagnetic wave absorption capacity of ACF. The previous analysis of the EM parameters shown in Figure 8 indicates that when the concentration of the Fe<sub>3</sub>O<sub>4</sub> particles is low, ACF-Fe<sub>3</sub>O<sub>4</sub>(1) has evident resonance peak at 6 GHz to 10 GHz, as shown in Figure 10(c),

and -45.9 dB appears at 6.9 GHz absorption peak. Figure 8(g) shows that when the thickness of the ACF-Fe<sub>3</sub>O<sub>4</sub>(3) composite coating is 2.0 mm, the reflection loss (RL) at 13–14.3 GHz and 15.1–16.1 GHz is below -10 dB (90% absorption), the minimum value is -15.2 dB at

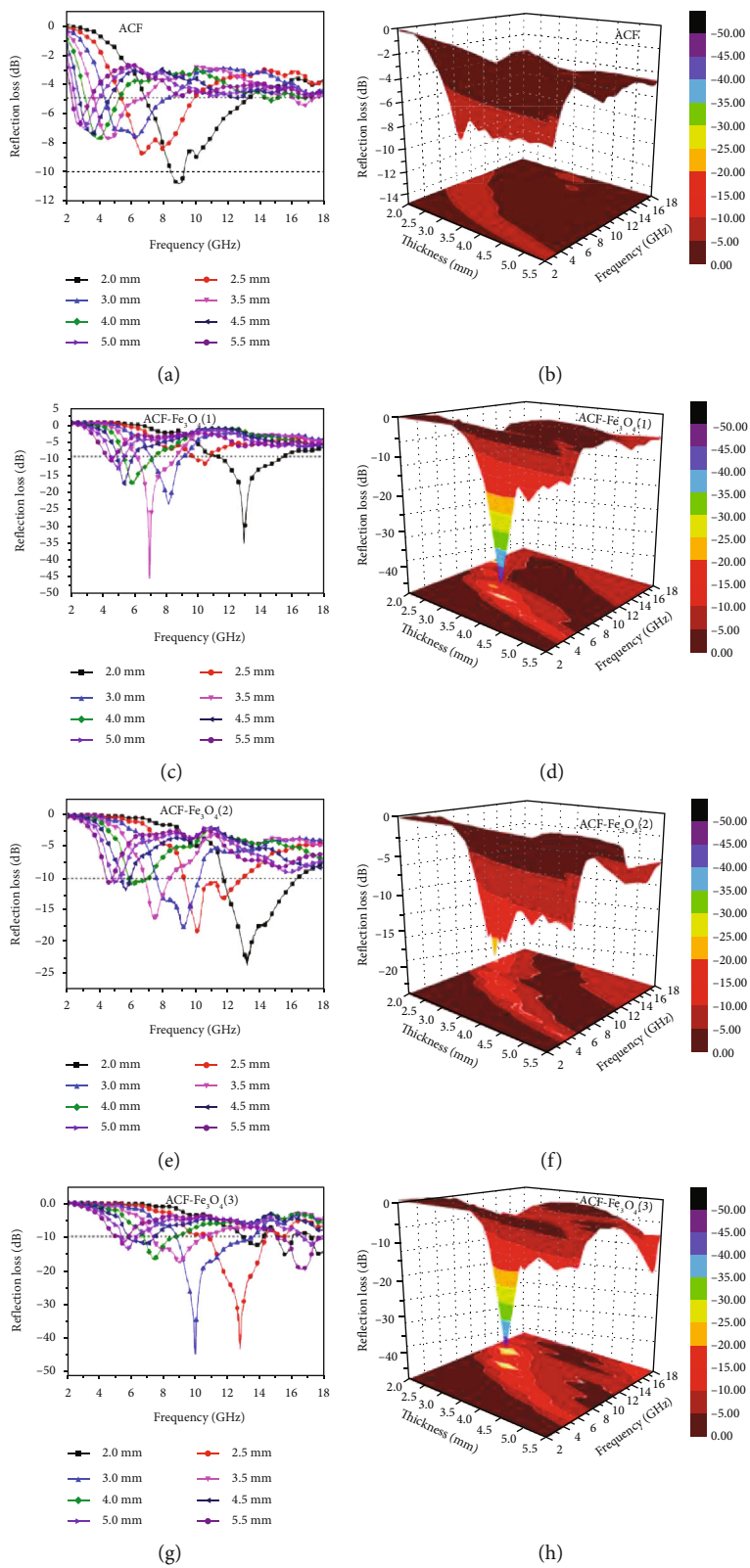


FIGURE 10: Continued.

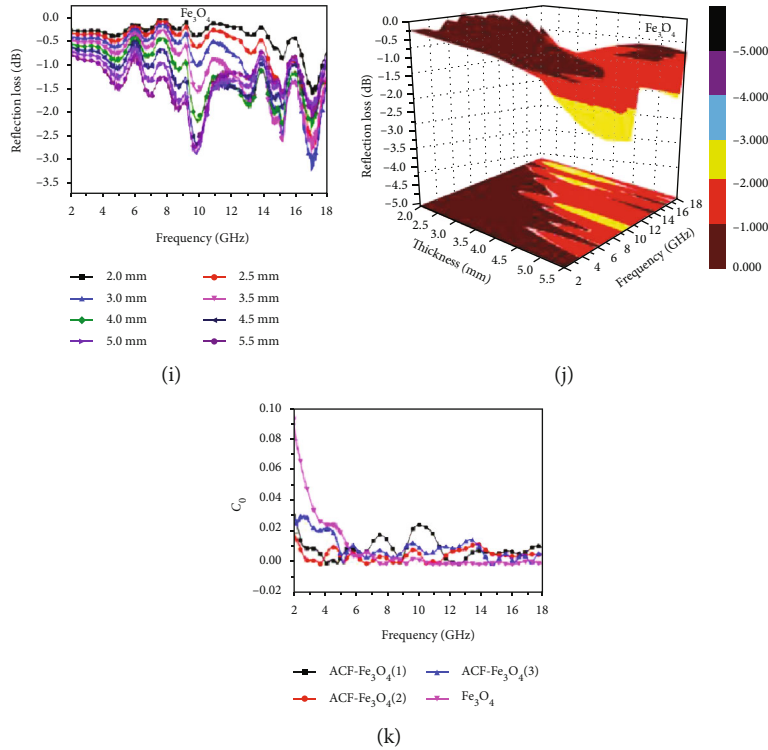


FIGURE 10: RL and 3D plots of ACF, ACF-Fe<sub>3</sub>O<sub>4</sub>(1), ACF-Fe<sub>3</sub>O<sub>4</sub>(2), ACF-Fe<sub>3</sub>O<sub>4</sub>(3), and pure Fe<sub>3</sub>O<sub>4</sub> over the 2–18 GHz range (a–i);  $C_0 - f$  curves of (k) Fe<sub>3</sub>O<sub>4</sub> and ACF-Fe<sub>3</sub>O<sub>4</sub> composites.

TABLE 2: Comparison of electromagnetic absorption properties of carbon/magnetic composites in the present and related studies.

Samples	Loading ratio (wt%)	Thickness (mm)	Electromagnetic wave absorption	References
Carbon fiber/nano-Fe <sub>3</sub> O <sub>4</sub>	50%	3.0	<-5 dB (8.9–9.5 GHz)	[44]
Carbon fiber/carbonyl iron	45%	2.0	<-10 dB (6.6–8.7 GHz)	[45]
Carbon fiber/Fe-Co	30%	2.0	<-10 dB (8.2–10.3 GHz)	[46]
Carbon fiber/Fe <sub>3</sub> O <sub>4</sub>	50%	4.41	<-10 dB (4.4–8.7 GHz)	[47]
PANI@Fe <sub>3</sub> O <sub>4</sub> @CNFs	15%	2.0	<-10 dB (11.9–15.6 GHz)	[48]
ACF/Fe <sub>3</sub> O <sub>4</sub> (3)	30%	3.0	<-10 dB (8.8–13.6 GHz)	Present work

15.6 GHz, and the bandwidth of the RL is below -10 dB is 2.3 GHz. As the layer thickness increases, the maximum RL moves significantly to a low frequency range. When the coating thickness reaches 3.0 mm, the corresponding ACF-Fe<sub>3</sub>O<sub>4</sub>(3) RL at 8.8–13.6 GHz is below -10 dB, while the minimum value at 10 GHz is -44.3 dB. The bandwidths corresponding to RLs below -10 dB and -20 dB (99% absorption) are 4.8 GHz and 1.1 GHz, respectively. The calculation results show that the synthesized ACF-Fe<sub>3</sub>O<sub>4</sub> composite material has better microwave absorption performance than the pure ACF and pure Fe<sub>3</sub>O<sub>4</sub> nanoparticles. Table 2 also shows the comparison of the electromagnetic wave absorption performance with other carbon/magnetic materials; the composite material prepared based on the porous ACF has obvious electromagnetic wave absorption performance. The loss caused by the Eddy current effect can be calculated by  $C_0(C_0 = \mu''(\mu')^{-2}f^{-1} = 2\pi\mu_0\sigma d^2/3)$ , where  $\sigma$  is the electrical conductivity,  $d$  is the diameter of the particle, and  $\mu'$  is the vacuum permeability. If the mag-

netic loss is caused by the Eddy loss effect, then  $C_0$  is constant when the frequency changes. Figure 10(k) shows the  $C_0 - f$  curve of the Fe<sub>3</sub>O<sub>4</sub> and ACF-Fe<sub>3</sub>O<sub>4</sub> composites. For pure Fe<sub>3</sub>O<sub>4</sub>, the  $C_0$  value is nearly constant in the frequency range of 6–18 GHz, while the change in  $C_0$  is only observed in the range of 2–6 GHz. When the amount of FeCl<sub>3</sub> added is 0.5 mol/L, two  $C_0$  levels remain in the range of 4–5 GHz and 14–18 GHz. However, at the 2–18 GHz frequency range,  $C_0$  shows a significant downward trend as the concentration of the FeCl<sub>3</sub> solution increases, particularly for ACF-Fe<sub>3</sub>O<sub>4</sub>(3). This characteristic means that pure Fe<sub>3</sub>O<sub>4</sub> has a significant Eddy current effect, which can be reduced by introducing ACF. In addition, the magnetic loss in ACF-Fe<sub>3</sub>O<sub>4</sub> is mainly caused by natural resonance and not caused by the Eddy current effect.

Numerous defects cause multiple scattering and interface polarization, thereby providing an important absorption mechanism. In addition, the fibrous structure and high specific surface properties of the ACF-Fe<sub>3</sub>O<sub>4</sub> composite material

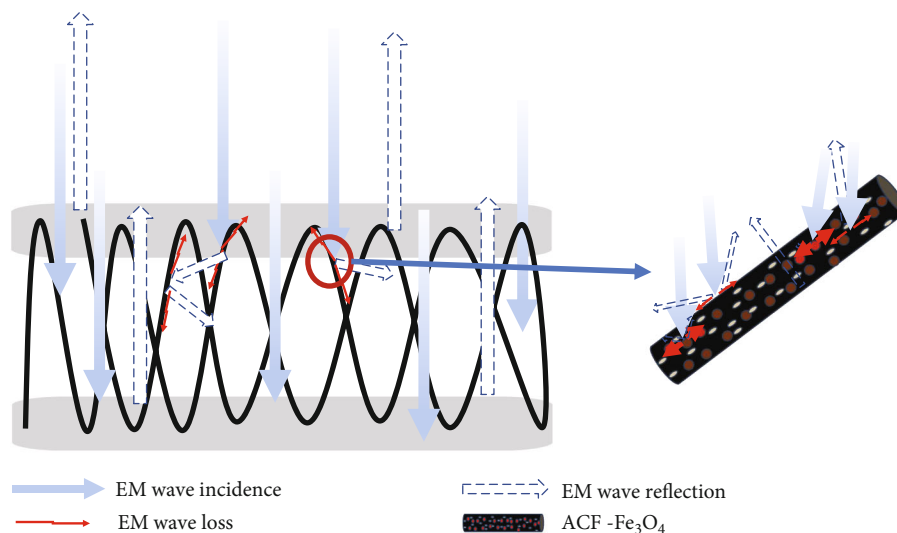


FIGURE 11: Scheme of the EM loss in the ACF- $\text{Fe}_3\text{O}_4$  composite felts.

may cause multiple reflections in the absorber. The result is an extended propagation path of the EM waves in the material, thereby further enhancing the absorption capacity of the composite material. Figure 11 shows a diagram that intuitively presents the EM wave absorption mechanism. In general, the enhanced of EM wave absorption performance of the composite materials is attributed to the compensation characteristics of ACF and  $\text{Fe}_3\text{O}_4$  that in the EM complementation effect previously proposed. Evidently, ACF- $\text{Fe}_3\text{O}_4$  composite material is a lightweight and efficient EM-absorbing material.

#### 4. Conclusions

This study selected ACF as a substrate and maximized its high specific surface area. By growing  $\text{Fe}_3\text{O}_4$  in situ on the surface of ACF, a high-efficiency, wide-band, and lightweight carbon magnetic EM wave-absorbing material based on ACF was prepared. ACF- $\text{Fe}_3\text{O}_4$  has more interfaces and defects, as well as multiple reflection losses, which in turn enhances the EM wave absorption performance. When the thickness of the prepared ACF- $\text{Fe}_3\text{O}_4$  is 3 mm, the minimum RL reached  $-44.3$  dB at 10 GHz, and the effective bandwidth of the RLs  $< -10$  dB and  $< -20$  dB is 4.8 GHz and 1.1 GHz, respectively. The prepared ACF- $\text{Fe}_3\text{O}_4$  has excellent properties such as broadband, high efficiency, stability, and lightness and is a new type of electromagnetic wave-absorbing composite material.

#### Data Availability

All data used to support the findings of this study are included within the article.

#### Conflicts of Interest

The authors declare that they have no competing interests.

#### Acknowledgments

This study was supported by the National Key Research and Development Program of China (2018YFC01810302) and a project funded by the Priority Academic Program Development of Jiangsu Higher Education Institutions (Su Caijiao [2018] No. 192).

#### References

- [1] W. Chen, S. Li, C. Chen, and L. Yan, "Self-assembly and embedding of nanoparticles by in situ reduced graphene for preparation of a 3D graphene/nanoparticle aerogel," *Advanced Materials*, vol. 23, no. 47, pp. 5679–5683, 2011.
- [2] C. Bao, L. Song, W. Xing et al., "Preparation of graphene by pressurized oxidation and multiplex reduction and its polymer nanocomposites by masterbatch-based melt blending," *Journal of Materials Chemistry*, vol. 22, no. 13, pp. 6088–6096, 2012.
- [3] X. Bai, Y. Zhai, and Y. Zhang, "Green approach to prepare graphene-based composites with high microwave absorption capacity," *Journal of Physical Chemistry C*, vol. 115, no. 23, pp. 11673–11677, 2011.
- [4] F. Peng, F. Meng, Y. Guo, H. Wang, F. Huang, and Z. Zhou, "Intercalating hybrids of sandwich-like  $\text{Fe}_3\text{O}_4$ -graphite: synthesis and their synergistic enhancement of microwave absorption," *ACS Sustainable Chemistry & Engineering*, vol. 6, no. 12, pp. 16744–16753, 2018.
- [5] J. Prasad, A. K. Singh, M. Tomar, V. Gupta, and K. Singh, "Strong electromagnetic wave absorption and microwave shielding in the Ni-Cu@MoS<sub>2</sub>/rGO composite," *Journal of Materials Science-Materials in Electronics*, vol. 30, no. 20, pp. 18666–18677, 2019.
- [6] P. He, Z.-L. Hou, K.-L. Zhang et al., "Lightweight ferroferric oxide nanotubes with natural resonance property and design for broadband microwave absorption," *Journal of Materials Science*, vol. 52, no. 13, pp. 8258–8267, 2017.
- [7] Y. Wan, J. Xiao, C. Li et al., "Microwave absorption properties of FeCo-coated carbon fibers with varying morphologies,"

- Journal of Magnetism and Magnetic Materials*, vol. 399, pp. 252–259, 2016.
- [8] X. Huang, J. Zhang, W. Rao, T. Sang, B. Song, and C. Wong, “Tunable electromagnetic properties and enhanced microwave absorption ability of flaky graphite/cobalt zinc ferrite composites,” *Journal of Alloys and Compounds*, vol. 662, pp. 409–414, 2016.
- [9] M. Ning, J. Li, B. Kuang et al., “One-step fabrication of N-doped CNTs encapsulating M nanoparticles (M = Fe, Co, Ni) for efficient microwave absorption,” *Applied Surface Science*, vol. 447, pp. 244–253, 2018.
- [10] W. Xie, H. Cheng, Z. Chu, Z. Chen, and C. Long, “Effect of carbonization temperature on the structure and microwave absorbing properties of hollow carbon fibres,” *Ceramics International*, vol. 37, no. 6, pp. 1947–1951, 2011.
- [11] Q. Sun, L. Sun, Y. Cai, T. Ji, and G. Zhang, “Activated carbon fiber/Fe<sub>3</sub>O<sub>4</sub> composite with enhanced electromagnetic wave absorption properties,” *RSC Advances*, vol. 8, no. 61, pp. 35337–35342, 2018.
- [12] H. Sun, R. Che, X. You et al., “Cross-stacking aligned carbon-nanotube films to tune microwave absorption frequencies and increase absorption intensities,” *Advanced Materials*, vol. 26, no. 48, pp. 8120–8125, 2014.
- [13] W. Ye, Q. Sun, and G. Zhang, “Effect of heat treatment conditions on properties of carbon-fiber-based electromagnetic-wave-absorbing composites,” *Ceramics International*, vol. 45, no. 4, pp. 5093–5099, 2019.
- [14] D. Wang, Z. Wang, X. Zheng, and M. Tian, “Activated carbon fiber derived from the seed hair fibers of *Metaplexis japonica*: novel efficient adsorbent for methylene blue,” *Industrial Crops and Products*, vol. 148, article 112319, 2020.
- [15] M. Cao, C. Han, X. Wang et al., “Graphene nanohybrids: excellent electromagnetic properties for the absorbing and shielding of electromagnetic waves,” *Journal of Materials Chemistry C*, vol. 6, no. 17, pp. 4586–4602, 2018.
- [16] L. Wang, Y. Huang, C. Li, J. Chen, and X. Sun, “Hierarchical graphene@Fe<sub>3</sub>O<sub>4</sub>nanocluster@carbon@MnO<sub>2</sub>nanosheet array composites: synthesis and microwave absorption performance,” *Physical Chemistry Chemical Physics*, vol. 17, no. 8, pp. 5878–5886, 2015.
- [17] C. Shi, J. Zhu, X. Shen et al., “Flexible inorganic membranes used as a high thermal safety separator for the lithium-ion battery,” *RSC Advances*, vol. 8, no. 8, pp. 4072–4077, 2018.
- [18] J. Qiu and T. Qiu, “Fabrication and microwave absorption properties of magnetite nanoparticle-carbon nanotube-hollow carbon fiber composites,” *Carbon*, vol. 81, pp. 20–28, 2015.
- [19] Y. Shao, W. Lu, H. Chen, J. Q. Xiao, Y. Qiu, and T.-W. Chou, “Flexible ultra-thin Fe<sub>3</sub>O<sub>4</sub>/MnO<sub>2</sub> core-shell decorated CNT composite with enhanced electromagnetic wave absorption performance,” *Composites Part B Engineering*, vol. 144, pp. 111–117, 2018.
- [20] L. Yan, C. Hong, B. Sun et al., “In situ growth of core–sheath heterostructural SiC nanowire arrays on carbon fibers and enhanced electromagnetic wave absorption performance,” *ACS Applied Materials & Interfaces*, vol. 9, no. 7, pp. 6320–6331, 2017.
- [21] Z. Zhou, C. Lai, L. Zhang et al., “Development of carbon nanofibers from aligned electrospun polyacrylonitrile nanofiber bundles and characterization of their microstructural, electrical, and mechanical properties,” *Polymer*, vol. 50, no. 13, pp. 2999–3006, 2009.
- [22] Z. Jiao and J. Qiu, “Microwave absorption performance of iron oxide/multiwalled carbon nanotubes nanohybrids prepared by electrostatic attraction,” *Journal of Materials Science*, vol. 53, no. 5, pp. 3640–3646, 2018.
- [23] H. Wang, P. Hu, D.’a. Pan, J. Tian, S. Zhang, and A. A. Volinsky, “Carbothermal reduction method for Fe<sub>3</sub>O<sub>4</sub> powder synthesis,” *Journal of Alloys and Compounds*, vol. 502, no. 2, pp. 338–340, 2010.
- [24] S. Qilong, S. Lei, C. Yingying et al., “Fe<sub>3</sub>O<sub>4</sub>-intercalated reduced graphene oxide nanocomposites with enhanced microwave absorption properties,” *Ceramics International*, vol. 45, no. 15, pp. 18298–18305, 2019.
- [25] K. Hina, H. Zou, W. Qian, D. Zuo, and C. Yi, “Preparation and performance comparison of cellulose-based activated carbon fibres,” *Cellulose*, vol. 25, no. 1, pp. 607–617, 2018.
- [26] X. Sun, J. He, G. Li et al., “Laminated magnetic graphene with enhanced electromagnetic wave absorption properties,” *Journal of Materials Chemistry C*, vol. 1, no. 4, pp. 765–777, 2013.
- [27] V. Shukla, “Role of spin disorder in magnetic and EMI shielding properties of Fe<sub>3</sub>O<sub>4</sub>/C/PPy core/shell composites,” *Journal of Materials Science*, vol. 55, no. 7, pp. 2826–2835, 2020.
- [28] C.-H. Ho, C.-P. Tsai, C.-C. Chung et al., “Shape-controlled growth and shape-dependent cation site occupancy of monodisperse Fe<sub>3</sub>O<sub>4</sub> nanoparticles,” *Chemistry of Materials*, vol. 23, no. 7, pp. 1753–1760, 2011.
- [29] X. Zhang, W. Zhu, W. Zhang, S. Zheng, and S. Qi, “Preparation of TiO<sub>2</sub>/Fe<sub>3</sub>O<sub>4</sub>/CF composites for enhanced microwave absorbing performance,” *Journal Of Materials Science-Materials In Electronics*, vol. 29, no. 9, pp. 7194–7202, 2018.
- [30] C. K. Lo, D. Xiao, and M. M. F. Choi, “Homocysteine-protected gold-coated magnetic nanoparticles: synthesis and characterisation,” *Journal of Materials Chemistry*, vol. 17, no. 23, p. 2418, 2007.
- [31] T. Yamashita and P. Hayes, “Analysis of XPS spectra of Fe<sup>2+</sup> and Fe<sup>3+</sup> ions in oxide materials,” *Applied Surface Science*, vol. 254, no. 8, pp. 2441–2449, 2008.
- [32] M. Ritter and W. Weiss, “Fe<sub>3</sub>O<sub>4</sub>(111) surface structure determined by LEED crystallography,” *Surface Science*, vol. 432, no. 1-2, pp. 81–94, 1999.
- [33] C. Sun, Y. Guo, X. Xu et al., “In situ preparation of carbon/Fe<sub>3</sub>C composite nanofibers with excellent electromagnetic wave absorption properties,” *Composites Part a-Applied Science and Manufacturing*, vol. 92, pp. 33–41, 2017.
- [34] L.-S. Zhong, J.-S. Hu, H.-P. Liang, A.-M. Cao, W.-G. Song, and L.-J. Wan, “Self-assembled 3D flowerlike iron oxide nanostructures and their application in water treatment,” *Advanced Materials*, vol. 18, no. 18, pp. 2426–2431, 2006.
- [35] X. J. Lee, H. N. Lim, N. S. K. Gowthaman, M. B. A. Rahman, C. A. Che Abdullah, and K. Muthoosamy, “In-situ surface functionalization of superparamagnetic reduced graphene oxide - Fe<sub>3</sub>O<sub>4</sub> nanocomposite via *Ganoderma lucidum* extract for targeted cancer therapy application,” *Applied Surface Science*, vol. 512, p. 145738, 2020.
- [36] W. Ye, Q. Sun, X. Long, and Y. Cai, “Preparation and properties of CF-Fe<sub>3</sub>O<sub>4</sub>-BN composite electromagnetic wave-absorbing materials,” *RSC Advances*, vol. 10, no. 19, pp. 11121–11131, 2020.
- [37] W. Ye, L. Sun, J. Yu, and X. Long, “Preparation and microwave absorption property of flexible lightweight&nbsp;magnetic particles-carbon fiber composites#br#,” *Journal of Textile Research*, vol. 40, no. 1, pp. 97–102, 2019.

- [38] Z. Han, D. Li, H. Wang et al., "Broadband electromagnetic-wave absorption by FeCo/C nanocapsules," *Applied Physics Letters*, vol. 95, no. 2, p. 023114, 2009.
- [39] J. Xiang, J. Li, X. Zhang, Q. Ye, J. Xu, and X. Shen, "Magnetic carbon nanofibers containing uniformly dispersed Fe/Co/Ni nanoparticles as stable and high-performance electromagnetic wave absorbers," *Journal of Materials Chemistry A*, vol. 2, no. 40, pp. 16905–16914, 2014.
- [40] M.-M. Lu, W.-Q. Cao, H.-L. Shi et al., "Multi-wall carbon nanotubes decorated with ZnO nanocrystals: mild solution-process synthesis and highly efficient microwave absorption properties at elevated temperature," *Journal of Materials Chemistry A*, vol. 2, no. 27, pp. 10540–10547, 2014.
- [41] M. S. Cao, R. R. Qin, C. J. Qiu, and J. Zhu, "Matching design and mismatching analysis towards radar absorbing coatings based on conducting plate," *Materials & Design*, vol. 24, no. 5, pp. 391–396, 2003.
- [42] J. Li, S. Bi, B. Mei et al., "Effects of three-dimensional reduced graphene oxide coupled with nickel nanoparticles on the microwave absorption of carbon fiberbased composites," *Journal of Alloys and Compounds*, vol. 717, pp. 205–213, 2017.
- [43] Y. Xiong and Y. Xia, "Shape-controlled synthesis of metal nanostructures: the case of palladium," *Advanced Materials*, vol. 19, no. 20, pp. 3385–3391, 2007.
- [44] H. Salimkhani, F. Movassagh-Alanagh, H. Aghajani, and K. Osouli-Bostanabad, "Study on the magnetic and microwave properties of electrophoretically deposited nano-Fe<sub>3</sub>O<sub>4</sub> on carbon fiber," *Procedia Materials Science*, vol. 11, pp. 231–237, 2015.
- [45] M.-J. Youh, H.-C. Wu, W.-H. Lin et al., "A carbonyl iron/carbon fiber material for electromagnetic wave absorption," *Journal of Nanoscience and Nanotechnology*, vol. 11, no. 3, pp. 2315–2320, 2011.
- [46] L. Wang, F. He, and Y. Wan, "Facile synthesis and electromagnetic wave absorption properties of magnetic carbon fiber coated with Fe-Co alloy by electroplating," *Journal of Alloys and Compounds*, vol. 509, no. 14, pp. 4726–4730, 2011.
- [47] C. Qiang, J. Xu, Z. Zhang et al., "Magnetic properties and microwave absorption properties of carbon fibers coated by Fe<sub>3</sub>O<sub>4</sub> nanoparticles," *Journal of Alloys and Compounds*, vol. 506, no. 1, pp. 93–97, 2010.
- [48] L. Yang, H. Cai, B. Zhang, S. Huo, and X. Chen, "Enhanced microwave absorption property of epoxy nanocomposites based on PANI@Fe<sub>3</sub>O<sub>4</sub>@CNFs nanoparticles with three-phase heterostructure," *Materials Research Express*, vol. 5, no. 2, 2018.